ACS APPLIED MATERIALS & INTERFACES

www.acsami.org

Research Article

Photoenhanced Electroresistance at Dislocation-Mediated Phase Boundary

Jing Wang,* Ruixue Zhu, Ji Ma, Huayu Yang, Yuanyuan Fan, Mingfeng Chen, Yuanwei Sun, Peng Gao, Houbing Huang, Jinxing Zhang, Jing Ma,* and Ce-Wen Nan

Cite This: *ACS Appl. Mater. Interfaces* 2022, 14, 18662−18670

Read Online

ACCESS | Metrics & More | Article Recommendations | Supporting Information

ABSTRACT: Ferroelectric tunneling junctions have attracted intensive research interest due to their potential applications in high-density data storage and neural network computing. However, the prerequisite of an ultrathin ferroelectric tunneling barrier makes it a great challenge to simultaneously implement the robust polarization and negligible leakage current in a ferroelectric thin film, both of which are significant for ferroelectric tunneling junctions with reliable operating performance. Here, we observe a large tunneling electroresistance effect of ~1.0 × 10^4% across the $BiFeO_3$ nanoisland edge, where the intrinsic ferroelectric polarization of the nanoisland makes a major contribution to tuning the barrier height. This phenomenon is beneficial from the artificially designed tunneling barrier between the nanoscale top electrode and the inclined conducting phase boundary, which is located between the rhombohedral-island and tetragonal-film matrix and arranged with the dislocation array. More significantly, the tunneling electroresistance effect is further improved to ~1.6 × 10^4% by the introduction of photoinduced carriers, which are separated by the flexoelectric field arising from the dislocations.

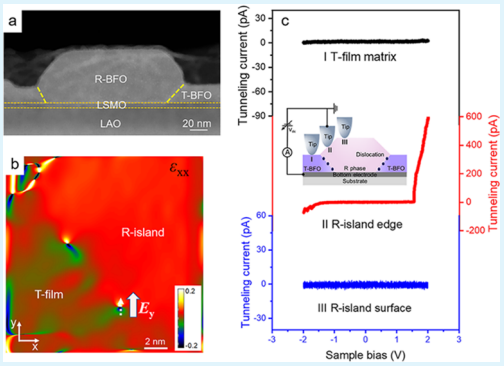

KEYWORDS: *ferroelectric tunneling junction, tunneling electroresistance effect, $BiFeO_3$ nanoislands, dislocations, flexoelectric effect*

INTRODUCTION

Ferroelectric tunneling junctions (FTJs) have attracted intensive research interest due to their applications in nonvolatile memories and synaptic devices with ultrafast and nondestructive read-out.[1−7] Superior to conventional insulators, ferroelectrics with spontaneous polarizations could effectively modulate the tunneling barrier's height and width,[8−10] resulting in a distinct and nonvolatile tunneling electroresistance (TER) effect. Additionally, the density of the storage data bits can be extremely high due to the availability of atomic-size domain engineering.[11] Unfortunately, ferroelectric catastrophe always occurs in the ultrathin film, which not only hinders the intrinsic ferroelectric tunneling behaviors by the formation of conduction filamentary[12,13] but also suppresses the switching of the ferroelectric polarization and hence the magnitude of TER. To date, people have taken great efforts to explore the possible methods to improve TER, such as replacing the metallic electrode with a semiconductor[4,5] and designing a ferroionic tunneling junction.[2] Moreover, the multiferroic tunneling barrier is also introduced to explore the four-state TER.[14−16] However, these approaches work only with very limited ferroelectric candidates, such as $BaTiO_3$,[4−7] $(Hf,Zr)O_2$[17] ultrathin films, or van der Waals layered ferroelectrics.[18,19]

Very recently, flexoelectricity[20] has been demonstrated to be capable of separation of photoinduced carriers and modifying the interfacial barrier profile,[21] giving rise to mechanical modulation of the ferroelectric quantum tunneling effect. Normally, flexoelectricity can be created in dielectric materials by applying a strain gradient via the nanoscale probe,[21−24] but the magnitude of the strain gradient (10^6−10^7 m^{-1}) and the flexoelectric field (~0.1−10 MV cm^{-1}) is largely restricted by the relative Young's modulus of the probe and the dielectric materials. However, a recent study has reported that a strain gradient with an even larger magnitude of ~10^8 m^{-1} is confirmed around the dislocation cores,[25] which implies that a large flexoelectricity naturally exists around them. The above analysis gives us a hint that a photoenhanced TER may be achieved when the ferroelectric tunneling behavior occurs across the dislocations, where a deterministic construction of reliable dislocations in ferroelectric thin films is highly required.

Taking advantage of the structural discrepancies between rhombohedral (R)- and tetragonal (T)-phase $BiFeO_3$ (BFO), as well as the successful growth of self-assembly BFO

Received: December 31, 2021
Accepted: April 5, 2022
Published: April 17, 2022

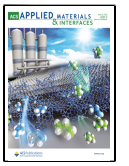

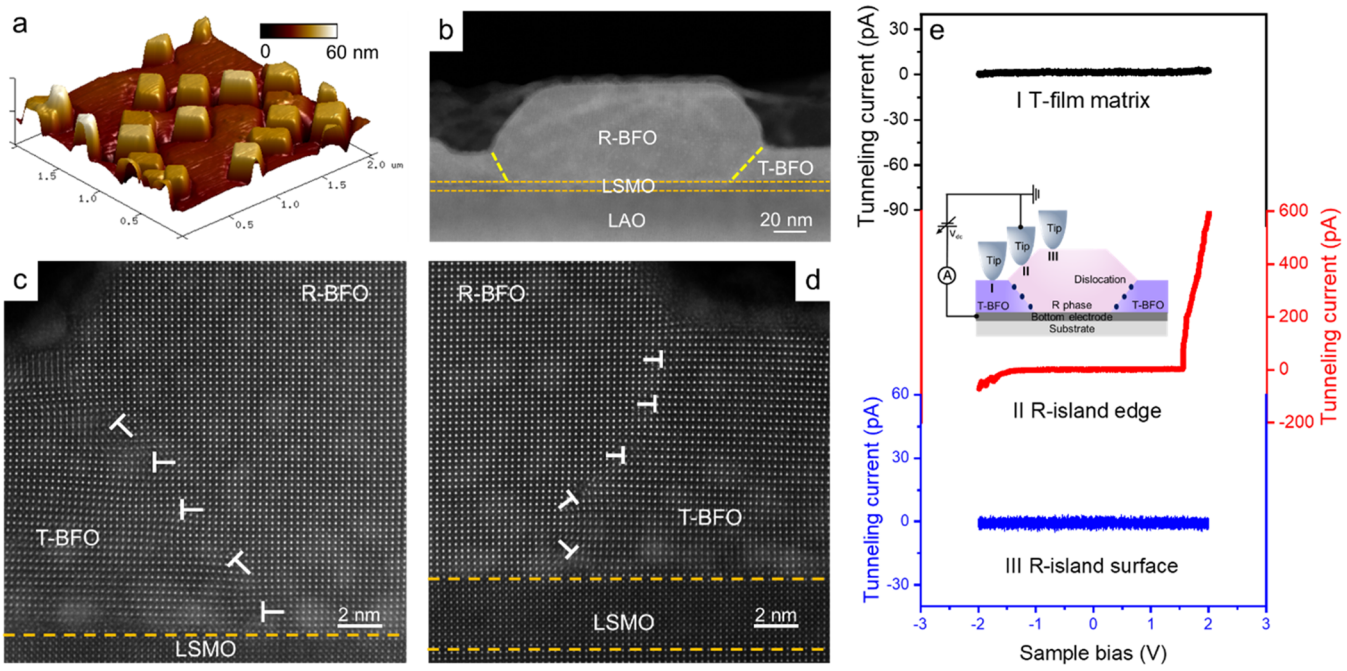

Figure 1. Large conduction obtained at the R-island edge with arrayed dislocations. (a) AFM image and (b) cross-sectional STEM image of the BFO nanoisland. (c, d) Atomic-resolution STEM image for the left- and right-hand side R-island/T-film interface. The "⊥"-shaped symbols indicate the dislocations arrayed at the interface. (e) $I-V$ curves obtained when the nanoscale probe is located at locations I, II, and III.

nanoislands, arrayed dislocations naturally form at the inclined interface between R-phase nanoislands (for simplicity, termed R-islands) and the T-phase thin-film matrix (termed T-film).[26,27] This model system provides us a good platform to explore the ferroelectric tunneling behaviors across the arrayed dislocations. Here, photoenhanced ferroelectric tunneling behaviors driven by flexoelectricity around the arrayed dislocations are investigated, where the tunneling junction is composed of a nanoscale probe, R-phase BFO, and the inclined boundary. By combination of piezoelectric force microcopy (PFM) and conducting-atomic force microscopy (c-AFM), distinct conductance states are confirmed to be related to the opposite out-of-plane polarization states. In addition, light-illumination-enhanced TER is further confirmed by homemade photoassisted conducting-atomic force microscopy (ph-AFM).[28,29] The flexoelectric field is investigated through geometric phase analysis (GPA). This study gives us a first glimpse of the light−matter interaction during the ferroelectric tunneling process and explores the avenue for FTJs with a thick tunneling barrier and robust polarizations.

RESULTS AND DISCUSSION

Self-assembled R-islands embedded in the T-film matrix were prepared on the $LaAlO_3$ (LAO) substrate, as shown in Figure 1, where a $(La,Sr)MnO_3$ (LSMO) buffer layer is pregrown for local transport measurements. The detailed growth mechanism for the self-assembled nanoislands has been provided in our previous work.[27] The top and cross-sectional morphologies of the nanoislands are characterized by atomic force microscopy (AFM) and high-resolution scanning transmission electron microscopy (STEM), as shown in Figure 1a,b, respectively. To further characterize the dislocation features at R-island/T-film interfaces, magnified STEM images with atomic resolution are carried out as shown in Figure 1c,d, where the dislocations are highlighted by "⊥"-shaped symbols.

To explore the proposed photomodulated electrical transport behaviors mediated by the interfacial dislocations, we first investigate the current−voltage ($I-V$) curves across the metallic probe/BFO/LSMO junction in a dark state, where the nanoscale probe is positioned on the top of the T-film matrix (case I), the middle edge (case II), and the top surface of the R-island (case III). The corresponding experimental setup and the $I-V$ curves are shown in Figure 1e. Here, it is noteworthy that the radius of the contact area is ∼10 nm,[22] which is much smaller than the length (∼50 nm) of the nanoisland edge. Thus, the tip can be positioned precisely on top of the three locations. According to the corresponding $I-V$ curves in Figure 1e, we clearly see that the dynamic conducting behavior is distinct for the different investigated locations. For the T-film matrix (case I), there is negligible conductance within the sweeping voltage range (see the black curve in Figure 1e), which is due to the large tunneling barrier across the T-film with ∼16 nm thickness, as illustrated by Figures 1b and S1a. Intriguingly, when the probe is positioned on top of the R-island edge (case II), an abrupt current increase is observed when the sweeping voltage approaches ∼1.6 V (see the red curve in Figure 1e), which is close to the positive coercive field as demonstrated in Figure S2. However, when the probe is located on the top of the R-island (case III), negligible conductance is observed once again (see the blue curve in Figure 1e), which is due to the large tunneling barrier of the R-island with a thickness of ∼60 nm, as illustrated by Figures 1b and S1b.

According to previous works,[30−34] the lattice discontinuity of the nanoscale ferroelectric entities (such as domain walls, phase boundaries, and dislocations) can induce the variation of the electronic structure[30] or accumulating charged defects,[35] which indicates the conducting characteristic of the inclined R-island/T-film interfaces (highlighted by the yellow dashed lines in Figure 1b) with arrayed dislocations. This deduction is further demonstrated by the small bidirectional conduction

https://doi.org/10.1021/acsami.1c25259
ACS Appl. Mater. Interfaces 2022, 14, 18662−18670

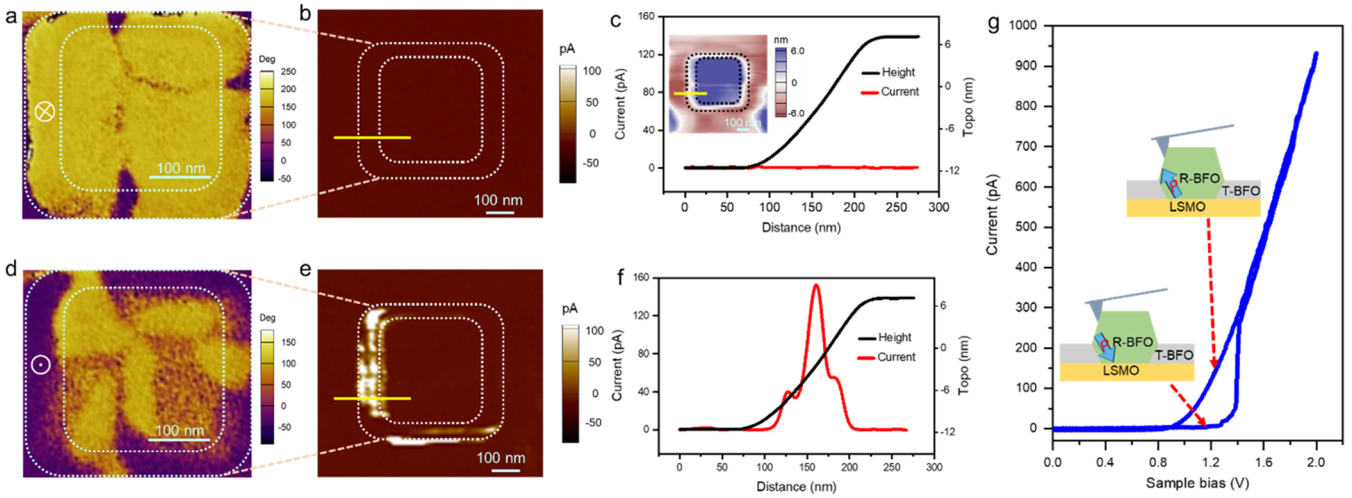

Figure 2. Quasi-static and dynamic tunneling conduction at the BFO R-island edge. (a) OOP PFM phase image for the initial downward domain pattern. The bright color and "⊗" symbol indicate the OOP downward polarization. (b) c-AFM current image for the nanoisland when the OOP polarization projection of the nanoisland edge is downward. (c) Current (indicated by the red curve) and topography (indicated by the black curve) profiles along the yellow line in (b) and (c), respectively. The inset shows the AFM image of the nanoisland. (d) OOP PFM phase image obtained after an upward 1.2 V is applied to the bottom electrode. The dark color and "⊙" symbol indicate the OOP upward polarization projection for the R-island edge. (e) c-AFM current image for the nanoisland when the OOP polarization projection for the R-island edge is upward. A read-out voltage of 1.2 V is applied to the bottom electrode. (f) Current (indicated by the red curve) and topography (indicated by the black curve) profiles along the yellow line in (e) and (c), respectively. (g) $I-V$ curve obtained at the R-island edge.

(~pA; see Figure S3) observed when the nanoscale probe is positioned close to the R-island/T-film interface. Hence, the conducting dislocations located along the inclined R-island/T-film interface decrease naturally the distance (~5 nm) of the electron transportation when the probe is located at the R-island edge, as schematically illustrated in Figure S4. This geometry allows to shrink the thickness of the tunneling layer but without decreasing the actual thickness of the ferroelectric nanoislands, which effectively avoids the leakage current. This physical schema explains the large conduction observed in case II (red curve in Figure 1e) with a point-contact geometry, but no observable conductance in cases I and III (black and blue curves in Figure 1e, respectively).

To have a deep understanding of the electronical transport behavior across the dislocations arrayed at the R-island/T-film interface with respect to the polarization orientations, the detailed conduction evolution of the nanoisland edge with out-of-plane (OOP) polarization projection changed from downward to upward is recorded, as shown in Figure 2, where the R-island edge is enclosed between the two dashed boxes. When the OOP polarization projection of the nanoisland edge points downward (indicated by the bright color and "⊗" symbol in the OOP PFM phase image in Figure 2a), no observable current is observed across the nanoisland edge in the c-AFM image in Figure 2b when a read-out voltage of 1.2 V is applied to the bottom electrode. The corresponding line profiles for the morphology (black curve) and current (red curve) across the nanoisland edge are shown in Figure 2c, where the inset shows the corresponding morphology of the investigated nanoisland. However, when the OOP polarization projection of the nanoisland edge is switched from downward to upward, as demonstrated by the dark color and the "⊙" symbol of the OOP phase image in Figure 2d, a dramatically enhanced current (~150 pA) is observed for the R-island edge (Figure 2e) with a read-out voltage of 1.2 V. The robust polarization switching of the nanoisland can be seen in Figure S5. The corresponding line profiles for the morphology (black curve) and current (red curve) across the nanoisland edge are shown in Figure 2f. These quasi-static current mapping images are consistent with the dynamic $I-V$ curve observed in Figure 2g. The illustration of asymmetric conduction of the nanoisland edges in Figure 2e can be seen in the Supporting Information Text and Figure S6. It is also notable that the observation in Figure 2 is a brand-new discovery, which is different from previous reports,[26,36,37] where their main focus was the electric field-controllable conduction states for the domain walls confined in the nanoislands with vertex-like quad-domain configurations. However, our present work mainly focuses on the tunneling conduction for the nanoisland edge, as indicated in Figure 2. The difference is, in previous works, the domain state of the whole nanoisland was either downward (high-resistance state; see Figure S7a,b) or upward (low-resistance state; see Figure S7e,f). However, in our work, only the polarization of the nanoisland edge is switched from the downward domain to the upward domain (low-resistance state), but the central part of the nanoisland remains downward (high-resistance state); please see Figure S7c,d. For all of the discussed cases, the domain state is controlled by the poling voltage applied on the scanning probe, as shown in Figure S7. Thus, we observed that only the edge is conducting but not the whole nanoisland.

Interestingly, the high conductance region embedded in the nanoisland edge shows ringlike stripes lapping around the nanoisland, as shown in Figure 2e, which can be explained by the orbicular distribution of the conducting dislocations at the R-island/T-film interfaces. This high conductance state is also observed repeatedly at the edges of the multiple nanoislands, as shown in Figure S8a, which further indicates that the large tunneling conduction is assisted by the conducting dislocations located at the R-island/T-film interface. Additionally, the c-AFM image with different scanning rates is also investigated, as shown in Figure S8a,b, to clarify the contributions of displacive current and DC current. The larger magnitude of the current in Figure S8b with a slower scanning rate of 0.8 μm s^{-1}

https://doi.org/10.1021/acsami.1c25259
ACS Appl. Mater. Interfaces 2022, 14, 18662−18670

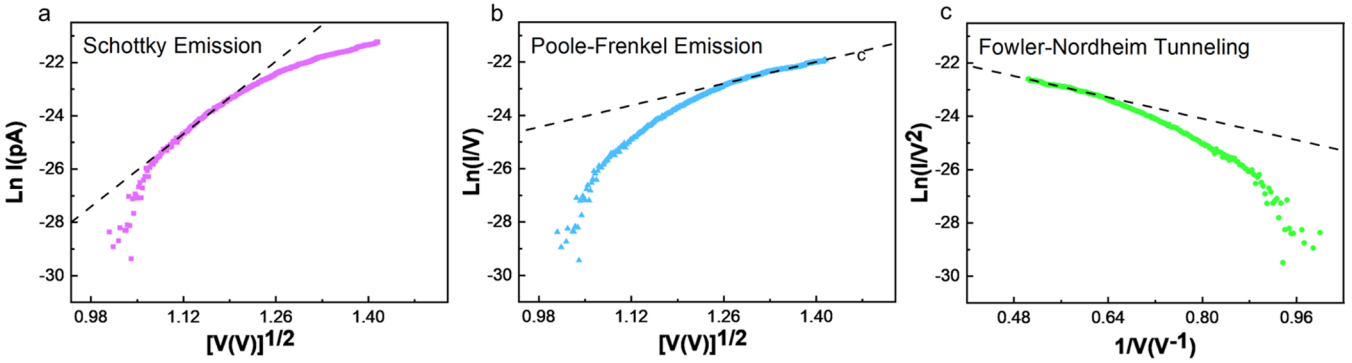

Figure 3. Conduction mechanism analysis for the electrical transport behavior obtained at the R-island edge. Data plotted in linear coordinates for the Schottky emission (a), the Poole−Frenkel emission (b), and the Fowler−Nordheim tunneling (c).

compared with the small current in Figure S8a with a faster scanning rate of 2 μm s^{-1} demonstrates that the current observed in the R-island edge results from the DC current contribution. Here, it is also noticeable that for both downward and upward polarization states of the R-island edge, the quantity of bound charges at the interfaces remains the same (as schematically illustrated by Figure S9); thus, the charged domain walls only contribute to the weak conduction (~pA) channel of the interface, as shown in Figure S3b, but not the large current (sub ~nA) observed in the red curve of Figure 1e.

Furthermore, the energy band structure is also drawn to understand the polarization-dependent electric transport behavior for this junction considering the conduction channel at the R/T boundary, as seen in the Supporting Information text and in Figure S10. The upward ferroelectric polarization of the T-phase film induces the downward band bending of the bottom of the conduction band and the top of the valance band of the conduction channel, as schematically shown in Figure S10a−d. After the electron tunneling from the Pt tip to R-BFO, the conduction channel with downward band bending makes electrons transport to the LSMO bottom electrode easily. According to the band structure and previous reports,[38−40] the electric transport behaviors are mainly determined by the Schottky barrier at the top interface.[38] When the polarization of R-BFO is downward, the Schottky barrier of the top interface increases (Figure S10e). In this case, it is challenging for electrons to tunnel from the probe to BFO, which is consistent with the negligible tunneling current in the experimental observation. However, when the polarization of R-BFO is upward, the Schottky barrier of the top interface decreases (Figure S10f), which is also consistent with our experimental observation of a large tunneling current in this case.

To understand the microscopic mechanism of the large conduction (low-resistance state) when the out-of-plane polarization projection is upward, multiple conduction mechanisms, including thermionic emission (Schottky emission), the Poole−Frenkel emission, and the Fowler−Nordheim tunneling models, are used to analyze the observed $I-V$ curve in Figure 2g within the backward-voltage-sweeping range. Here, the Schottky emission is as follows[41]

$$I_S = A_{eff} A T^2 \exp\left[\frac{\Phi}{k_b T} - \frac{e}{k_b T}\left(\frac{eE}{4\pi\varepsilon\varepsilon_0}\right)^{1/2}\right] \quad (1)$$

where A is the Richardson coefficient, A_{eff} is the effective contact area, Φ is the Schottky barrier height, e is the electronic charge, ε is the dielectric constant, and E is the applied field. The Poole−Frenkel emission is as follows[42]

$$I_{FP} \propto A_{eff} E \exp\left(\frac{-e(\Phi_0 - \sqrt{eE/\pi\varepsilon\varepsilon_0})}{k_b T}\right) \quad (2)$$

where Φ_0 is the barrier height that an electron must cross to move from one atom to another in the crystal. Last, the Fowler−Nordheim tunneling is as follows[38]

$$I_{FN} = A_{eff}\frac{e^3 m_{Pt}}{8\pi h m_{BFO}\phi_B} \times E^2 \exp\left(-\frac{8\pi\sqrt{2m_{BFO}}}{3he}\frac{\phi_B^{3/2}}{E}\right) \quad (3)$$

which is a function of the barrier height, ϕ_B; electric field, E; effective tunneling area, A_{eff}; and the effective electron mass in the tip (m_{Pt}) and in the BFO (m_{BFO}). According to the results summarized in Figure 3, we conclude that the Schottky emission is dominant at the small electric field and the Poole−Frenkel emission or the Fowler−Nordheim tunneling is dominant at the large electric field.

Before we further explore the photomodulated electroresistance effect in this point-contact geometry, we first investigate the flexoelectric field across the dislocations located at the R-island/T-film interface, which is based on the GPA mapping of both the in-plane (IP) strain (ε_{xx}) and the OOP strain (ε_{yy}) distribution for the dislocations. Figure 4a,d shows the GPA maps for the left-hand-side boundary along the $LAO_{[100]pc}$ and $LAO_{[001]pc}$ directions, respectively. Intriguingly, it only shows two dislocation features in the GPA map of ε_{xx} (see Figure 4a), which is because only these two dislocations show the Burgers vector with OOP projection, as marked by the "⊥"-shaped symbols in Figure 1c. Line profile is performed across one dislocation, as shown in Figure 4b, which is along the white dashed arrow in Figure 4a. A sudden change of ε_{xx} from ~ −0.8% (close to the T-film region) to ~1.0% (close to the R-island region) occurs within ~0.1 nm distance, as shown in Figure 4b, which accompanies a maximum strain gradient ($\delta\varepsilon_{xx}/\delta l$) of ~ 5.0×10^8 m^{-1} across the dislocation core. However, for the GPA map of ε_{yy} for the dislocations, all of the dislocations show strain mutation, as shown in the sharp color contrast in Figure 4d. An abrupt strain variation from ~2.3% (close to the T-film region) to ~ −2.4% (close to the R-island region) is observed according to the line profile in Figure 4e, which is along the white dashed arrow in Figure 4d. The

https://doi.org/10.1021/acsami.1c25259
ACS Appl. Mater. Interfaces 2022, 14, 18662−18670

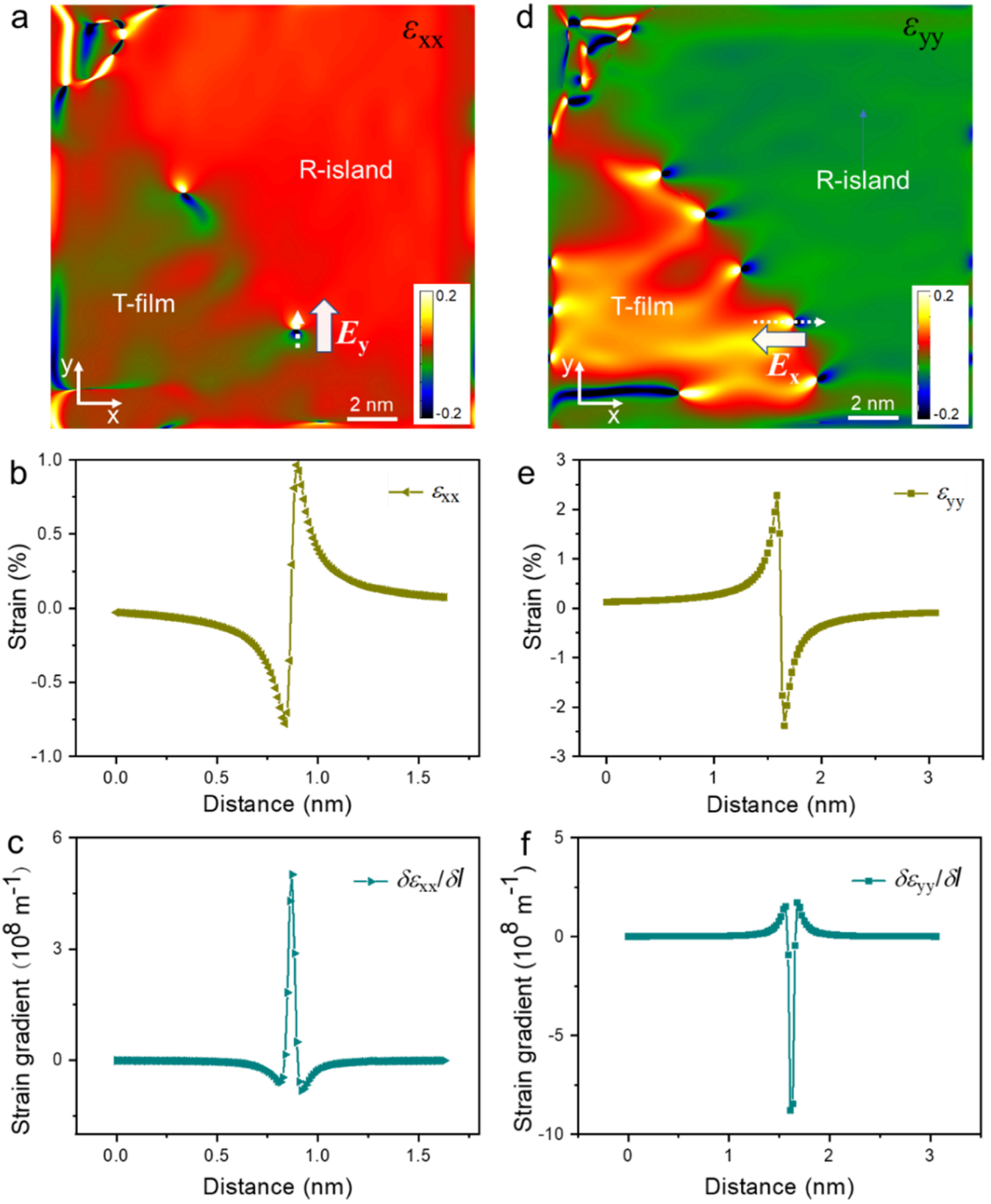

Figure 4. Large strain gradient observed at dislocation cores. (a) IP strain (ε_{xx}) and (d) OOP strain (ε_{yy}) map obtained by GPA analysis, where x is parallel to the $LAO_{[100]pc}$ direction and y is parallel to the $LAO_{[001]pc}$ direction. (b) IP strain (ε_{xx}) and (e) OOP strain (ε_{yy}) distribution across the dislocation along the white dashed arrow in (a) and (d), respectively. (c) IP strain gradient ($\delta\varepsilon_{xx}/\delta l$) and (f) OOP strain gradient ($\delta\varepsilon_{yy}/\delta l$) distribution across the dislocation along the white dashed arrow in (a) and (d), respectively.

corresponding maximum strain gradient ($\delta\varepsilon_{yy}/\delta l$) approaches $\sim -8.8 \times 10^8$ m^{-1} across the dislocation core. Simultaneously, similar results for the maximum strain gradients of $\sim 1.3 \times 10^8$ m^{-1} for $\delta\varepsilon_{xx}/\delta l$ and $\sim 8.1 \times 10^7$ m^{-1} for $\delta\varepsilon_{yy}/\delta l$ around the dislocations arrayed along the right-hand-side boundary are confirmed, as shown in Figure S11. The strain changes its sign abruptly through the dislocation core within only a few angstrom width (Figures 4b,e and S11b,e), which naturally results in a much larger magnitude of strain gradient ($\sim 10^8$ m^{-1}) compared with the counterpart in thin films induced by the nanoscale probe ($\sim 10^7$ m^{-1})[21,22] or the morphotropic phase boundaries (10^6 m^{-1}).[43,44] Therefore, according to the equation of the flexoelectric field[20]

$$E_{\text{flexo}} = \frac{e}{4\pi\varepsilon_0 a}\frac{\partial u}{\partial z} \tag{4}$$

where e is the electronic charge, ε_0 is the permittivity of free space, and $\partial u/\partial z$ is the strain gradient, large E_{flexo} values of ~ 19 and ~ 33 MV cm^{-1} are deduced from the maximum strain gradient for $\delta\varepsilon_{xx}/\delta l$ in Figure 4c and $\delta\varepsilon_{yy}/\delta l$ in Figure 4f, which are indicated by the white arrow in Figure 4a,d. According to

https://doi.org/10.1021/acsami.1c25259
ACS Appl. Mater. Interfaces 2022, 14, 18662−18670

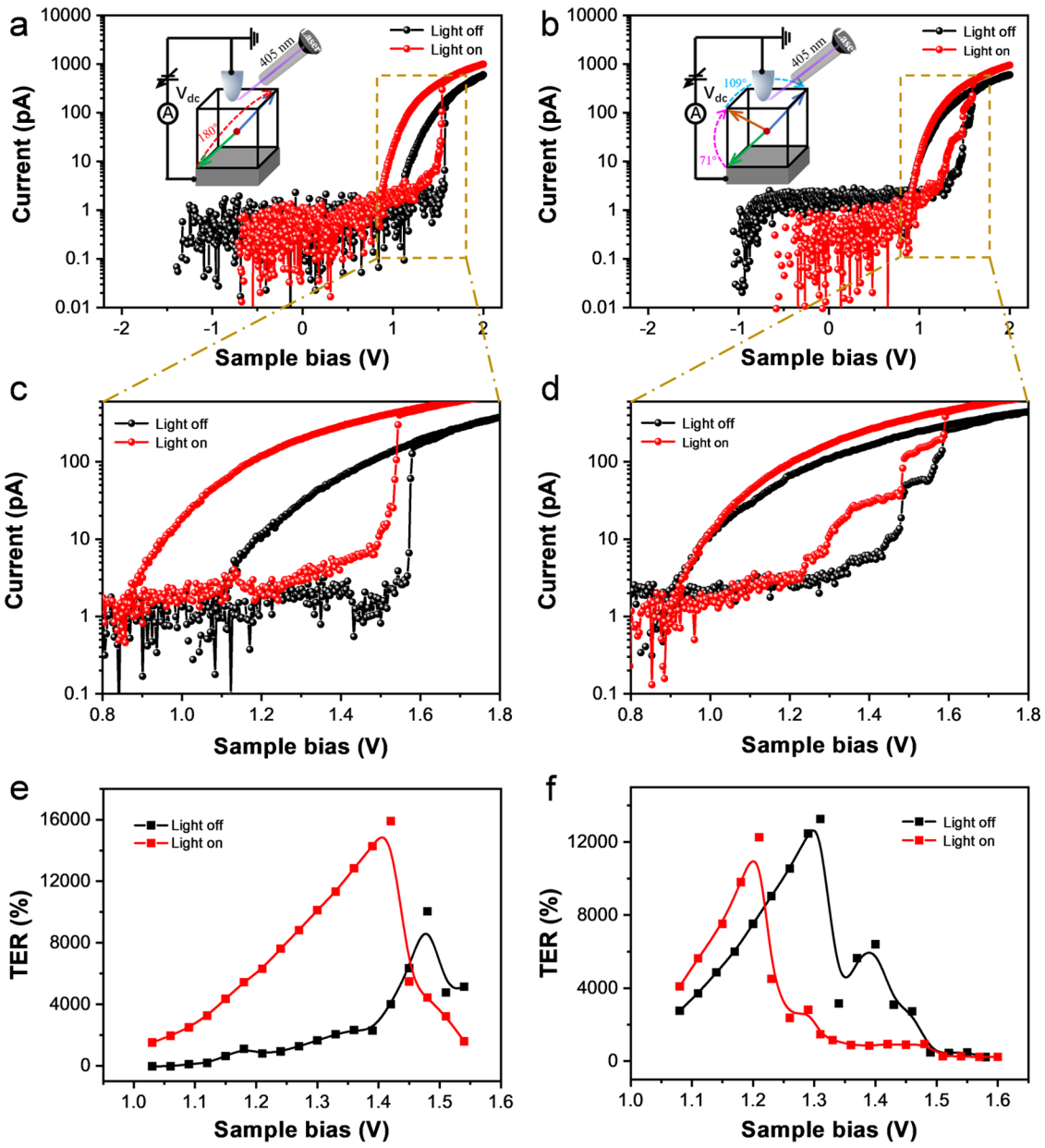

Figure 5. Ferroelectric switching pathway-dependent tunneling conductance without/with light illumination. (a) One-step and (b) two-step tunneling $I-V$ hysteresis curves without (black curve)/with (red curve) light illumination. The insets show the corresponding schematics for the one-step and two-step ferroelectric switching processes. Distinct tunneling behaviors are obtained at different locations of the R-island edge. (c, d) Magnified $I-V$ curve for the part enclosed by the dashed box in a and b, respectively. (e, f) TER for one-step (c) and two-step tunneling (d) without (black curve)/with (red curve) light illumination.

previous reports,[21,22,31] a large flexoelectric field can also induce a substantial photoconduction by separation of the photoinduced electron−hole pairs, which will further improve the TER of FTJ by polarization-dependent light-illumination-induced modulation of the tunneling barrier.[45] Thus, a large TER between the nanoscale probe and the dislocations is expected due to the localized large flexoelectric field from the dislocations. In addition, considering that the photoinduced electrons are transported from the nanoscale probe to the bottom LSMO electrode, the flexoelectric field along the $LAO_{[001]pc}$ orientation (as shown in Figure 4a) generated by the dislocations should make the major contribution to the photomodulated electrical transport behavior.

When a light is illuminated between the nanoscale probe and the R-island edge, the tunneling current arises from two contributions: one is the intrinsic tunneling current at the dark and the other is from the flexoelectric field separated photocarriers, which can be expressed as follows

$$I_t = I_{dark} + I_{ph} \tag{5}$$

where the dark current (I_{dark}) can be estimated using the Poole−Frenkel emission or the Fowler−Nordheim tunneling modeling as we discussed above. For both cases, the applied electric field (E) arises from the external electric field (E) applied by c-AFM. In addition, the contribution from light illumination to the tunneling current (I_{Ph}) arises from the modulation of the tunneling barrier[21,28] by the photoinduced

https://doi.org/10.1021/acsami.1c25259
ACS Appl. Mater. Interfaces 2022, 14, 18662−18670

carriers separated by the flexoelectric field, where the corresponding current density for the flexo-photovoltaic effect can be expressed as follows[31]

$$J_{FVP} = G\alpha I_0 \quad (6)$$

where G and α are the Glass coefficient ($\sim 10^{-9}$ cm V^{-1} [31]) and the light absorption coefficient ($\sim 1 \times 10^5$ cm^{-1})[46] of BFO, respectively, and I_0 is the light intensity (8 mW cm^{-2} in this work).

Based on the above analysis, we then compare the tunneling conductance at the edge of the nanoisland in the dark and with light illumination. Typically, two types of $I-V$ curves with different polarization switching pathways (e.g., one-step 180° switching and two-step 71 → 109° switching[39,47,48]) across the R-island edge are confirmed during the ferroelectric tunneling process, as shown in Figure 5a,b and the corresponding schematics. The asymmetry of the $I-V$ curve may arise from the fact that the Schottky barrier only forms at the top Pt probe/BFO interface due to the large work function of Pt (5.3 eV).[49] However, it is nonblocking at the bottom interface due to the similar work functions of (La,Sr)MnO_3 (4.7 eV) and $BiFeO_3$ (4.7 eV).[49] The $I-V$ curves characterized by c-AFM exhibit a one-step abrupt enhanced tunneling current without light illumination (black curve), as shown in the magnified $I-V$ curve of Figure 5c, which occurs at an external electric field of 1.57 V. When a 405 nm light with an intensity of 8 mW/cm^2[28] is illuminated at the interface of the probe/R-island edge, the ferroelectric tunneling behavior occurs at a smaller voltage (1.54 V), and the abrupt tunneling current is enhanced by 2.7 times. For the ferroelectric tunneling process accompanied by 71 → 109° polarization switching in the magnified data of Figure 5d, the $I-V$ curve shows a two-step abrupt enhanced tunneling current, both in the dark state and under the light illumination. To further quantitatively compare the tunneling conduction in the dark and under light illumination, TER is counted for the cases of one-step and two-step tunneling without/with light illumination, as shown in Figure 5e,f, respectively. Here, TER is defined as $\frac{I_{backward} - I_{forward}}{I_{forward}}$ at one specific sweeping voltage. For the one-step tunneling under light illumination, nonconduction was observed for OOP downward polarizations when the electric field was smaller than ~1.43 V, while it was gradually and then dramatically enhanced when the electric field was swept close to the switching field and consequently backward. This phenomenon directly explains the first enhancement (the maximum value is $\sim 1.6 \times 10^4$%) and then the depression of TER compared with that in the case of the dark state. However, for the two-step tunneling, the current increases obviously close to 71° switching and continuously increases between 71 and 109° switching during the forward voltage sweeping. Therefore, although the current is also enhanced obviously during the backward voltage sweeping, the TER is not superior compared with the dark state. Here, we can conclude that compared with two-step polarization switching, the photoenhanced TER effect is more easily implemented for one-step polarization switching.

CONCLUSIONS

In summary, ferroelectric tunneling behaviors are demonstrated to occur between the nanoscale probe and the BFO structural-variant-mediated interface, where the intrinsic ferroelectric polarization makes the major contribution to tuning the tunneling barrier. The flexoelectric field arising from the arrayed dislocations located at the inclined interface helps promote the TER effect ($\sim 1.6 \times 10^4$%) by the separation of photoinduced carriers. This study provides a deep understanding of the electron tunneling behavior across a dislocation-mediated ferroelectric barrier, which provides a new strategy to construct ferroelectric tunneling junctions with an enhanced TER effect.

METHODS

Nanoisland Growth. BFO thin films were grown on LAO (001) single-crystal substrates with a LSMO bottom electrode by the pulsed laser deposition technique. During the thin-film growth, the laser energy and repetition rate were ~1.5 J cm^{-2} and 5 Hz, respectively. In addition, the thin films were grown at 700 °C under an oxygen pressure of 0.2 mbar. After deposition, the films were slowly cooled under an oxygen pressure of 200 mbar.

AFM, PFM, and c-AFM/Ph-AFM Measurements. AFM, PFM, and c-AFM/Ph-AFM experiments were performed at ambient conditions with Infinity Asylum Research AFM and Bruker AFM. A commercial Pt/Ir-coated tip on a Si cantilever (tip radius of 20 nm, force constant of 2.8 N m^{-1}, and a resonant frequency of 75 kHz) was used as the top electrode to characterize the ferroelectric domain patterns and conductivity. The amplitude and frequency of the actuating signal were 1.0 V_{pp} and 384 kHz, respectively.

High-Angle Annular Dark-Field Imaging-STEM (HAADF-STEM) and GPA Characterizations. The cross-sectional TEM samples of the BFO films were fabricated through a series of processes including manual slicing, gluing, grinding, and subsequent mechanical argon-ion milling using PIPS (Model 691, Gatan Inc.). Low voltage (0.5 kV) and low angle (±2°) were used in the final stage of the milling process to remove the surface damage caused by the ion beam. Atomically resolved HAADF-STEM images were acquired using an aberration-corrected FEI Titan Themis G2, with a spatial resolution of 60 pm, and operating at 300 kV. A convergence semiangle of 30 mrad was used here for imaging. Geometric phase analyses were performed on the atomic image using plugins in the Gatan Digital Micrograph platform.

ASSOCIATED CONTENT

Supporting Information

The Supporting Information is available free of charge at https://pubs.acs.org/doi/10.1021/acsami.1c25259.

Additional experimental data, including PFM and c-AFM images, GPA analysis for the nanoisland, as well as the energy band diagram of the proposed ferroelectric tunneling junction (PDF)

AUTHOR INFORMATION

Corresponding Authors

Jing Wang − *Advanced Research Institute of Multidisciplinary Science, and School of Materials Science & Engineering, Beijing Institute of Technology, Beijing 100081, China; State Key Laboratory of New Ceramics and Fine Processing, School of Materials Science and Engineering, Tsinghua University, Beijing 100084, China;* orcid.org/0000-0002-9099-7339; Email: jwang@bit.edu.cn

Jing Ma − *State Key Laboratory of New Ceramics and Fine Processing, School of Materials Science and Engineering, Tsinghua University, Beijing 100084, China*; Email: majing@mail.tsinghua.edu.cn

Authors

Ruixue Zhu − *International Center for Quantum Materials, and Electron Microscopy Laboratory, School of Physics, Peking University, Beijing 100871, China*

https://doi.org/10.1021/acsami.1c25259
ACS Appl. Mater. Interfaces 2022, 14, 18662−18670

Ji Ma − *State Key Laboratory of New Ceramics and Fine Processing, School of Materials Science and Engineering, Tsinghua University, Beijing 100084, China; School of Material Science and Engineering, Kunming University of Science and Technology, Kunming, Yunnan 650093, China*

Huayu Yang − *Advanced Research Institute of Multidisciplinary Science, and School of Materials Science & Engineering, Beijing Institute of Technology, Beijing 100081, China*

Yuanyuan Fan − *Advanced Research Institute of Multidisciplinary Science, and School of Materials Science & Engineering, Beijing Institute of Technology, Beijing 100081, China*

Mingfeng Chen − *State Key Laboratory of New Ceramics and Fine Processing, School of Materials Science and Engineering, Tsinghua University, Beijing 100084, China;* orcid.org/0000-0001-8408-0359

Yuanwei Sun − *International Center for Quantum Materials, and Electron Microscopy Laboratory, School of Physics, Peking University, Beijing 100871, China*

Peng Gao − *International Center for Quantum Materials, and Electron Microscopy Laboratory, School of Physics, Peking University, Beijing 100871, China;* orcid.org/0000-0003-0860-5525

Houbing Huang − *Advanced Research Institute of Multidisciplinary Science, and School of Materials Science & Engineering, Beijing Institute of Technology, Beijing 100081, China;* orcid.org/0000-0002-8006-3495

Jinxing Zhang − *Department of Physics, Beijing Normal University, Beijing 100875, China;* orcid.org/0000-0001-8977-5678

Ce-Wen Nan − *State Key Laboratory of New Ceramics and Fine Processing, School of Materials Science and Engineering, Tsinghua University, Beijing 100084, China*

Complete contact information is available at: https://pubs.acs.org/10.1021/acsami.1c25259

Author Contributions

J.W. and R.Z. contributted equally to this work. J.W. and J.M. conceived the project. J.M. and M.C. fabricated the thin films. J.W., H.Y., and Y.F. performed PFM and c-AFM/ph-AFM measurements. R.Z. and Y.S. performed TEM measurements and GPA under the supervision of P.G. J.W. wrote the first draft of the manuscript. All authors discussed the results and edited the manuscript.

Notes

The authors declare no competing financial interest.

■ ACKNOWLEDGMENTS

This work was supported by the National Natural Science Foundation of China (NSFC) grant 12004036, 51922055, the Basic Science Center Program of the National Natural Science Foundation of China (NSFC) grant 51788104 and the Beijing Institute of Technology Research Fund Program for Young Scholars. J.Z. also acknowledges the Foundation of Hubei Key Laboratory of Ferro & Piezoelectric Materials and Devices (K201902). The authors are also grateful to the Analysis & Testing Center at BIT.

■ REFERENCES

(1) Chanthbouala, A.; Crassous, A.; Garcia, V.; Bouzehouane, K.; Fusil, S.; Moya, X.; Allibe, J.; Dlubak, B.; Grollier, J.; Xavier, S.; Deranlot, C.; Moshar, A.; Proksch, R.; Mathur, N. D.; Bibes, M.; Barthélémy, A. Solid-State Memories Based on Ferroelectric Tunnel Junctions. *Nat. Nanotechnol.* **2012**, *7*, 101−104.

(2) Li, J.; Li, N.; Ge, C.; Huang, H.; Sun, Y.; Gao, P.; He, M.; Wang, C.; Yang, G.; Jin, K. Giant Electroresistance in Ferroionic Tunnel Junctions. *iScience* **2019**, *16*, 368−377.

(3) Ma, C.; Luo, Z.; Huang, W.; Zhao, L.; Chen, Q.; Lin, Y.; Liu, X.; Chen, Z.; Liu, C.; Sun, H.; Jin, X.; Yin, Y.; Li, X. Sub-Nanosecond Memristor Based on Ferroelectric Tunnel Junction. *Nat. Commun.* **2020**, *11*, No. 1439.

(4) Wen, Z.; Li, C.; Wu, D.; Li, A.; Ming, N. Ferroelectric-Field-Effect-Enhanced Electroresistance in Metal/Ferroelectric/Semiconductor Tunnel Junctions. *Nat. Mater.* **2013**, *12*, 617−621.

(5) Xi, Z.; Ruan, J.; Li, C.; Zheng, C.; Wen, Z.; Dai, J.; Li, A.; Wu, D. Giant Tunnelling Electroresistance in Metal/Ferroelectric/Semiconductor Tunnel Junctions by Engineering the Schottky Barrier. *Nat. Commun.* **2017**, *8*, No. 15217.

(6) Yin, Y. W.; Burton, J. D.; Kim, Y. M.; Borisevich, A. Y.; Pennycook, S. J.; Yang, S. M.; Noh, T. W.; Gruverman, A.; Li, X. G.; Tsymbal, E. Y.; Li, Q. Enhanced Tunnelling Electroresistance Effect Due to a Ferroelectrically Induced Phase Transition at a Magnetic Complex Oxide Interface. *Nat. Mater.* **2013**, *12*, 397−402.

(7) Wen, Z.; Wu, D. Ferroelectric Tunnel Junctions: Modulations on the Potential Barrier. *Adv. Mater.* **2019**, *13*, No. e1904123.

(8) Zhuravlev, M. Y.; Sabirianov, R. F.; Jaswal, S. S.; Tsymbal, E. Y. Giant Electroresistance in Ferroelectric Tunnel Junctions. *Phys. Rev. Lett.* **2005**, *94*, No. 169901E.

(9) Kohlstedt, H.; Pertsev, N. A.; Contreras, J. R.; Waser, R. Theoretical Current-Voltage Characteristics of Ferroelectric Tunnel Junctions. *Phys. Rev. B: Condens. Matter Mater. Phys.* **2005**, *72*, No. 125341.

(10) Tsymbal, E. Y.; Kohlstedt, H. Applied Physics. Tunneling across a Ferroelectric. *Science* **2006**, *313*, 181.

(11) Lee, H. J.; Lee, M.; Lee, K.; Jo, J.; Yang, H.; Kim, Y.; Chae, S. C.; Waghmare, U.; Lee, J. H. Scale-Free Ferroelectricity Induced by Flat Phonon Bands in Hfo2. *Science* **2020**, *369*, 1343−1347.

(12) Szot, K.; Speier, W.; Bihlmayer, G.; Waser, R. Switching the Electrical Resistance of Individual Dislocations in Single-Crystalline Srtio3. *Nat. Mater.* **2006**, *5*, 312−320.

(13) Silva, J. P. B.; Kamakshi, K.; Sekhar, K. C.; Moreira, J. A.; Almeida, A.; Pereira, M.; Gomes, M. J. M. Ferroelectric Polarization and Resistive Switching Characteristics of Ion Beam Assisted Sputter Deposited Batio3 Thin Films. *J. Phys. Chem. Solids* **2016**, *92*, 7−10.

(14) Gajek, M.; Bibes, M.; Fusil, S.; Bouzehouane, K.; Fontcuberta, J.; Barthélémy, A.; Fert, A. Tunnel Junctions with Multiferroic Barriers. *Nat. Mater.* **2007**, *6*, 296−302.

(15) Pantel, D.; Goetze, S.; Hesse, D.; Alexe, M. Reversible Electrical Switching of Spin Polarization in Multiferroic Tunnel Junctions. *Nat. Mater.* **2012**, *11*, 289−293.

(16) Garcia, V.; Bibes, M.; Bocher, L.; Valencia, S.; Kronast, F.; Crassous, A.; Moya, X.; Enouz-Vedrenne, S.; Gloter, A.; Imhoff, D.; et al. Ferroelectric Control of Spin Polarization. *Science* **2010**, *327*, 1106−1110.

(17) Cheema, S. S.; Kwon, D.; Shanker, N.; Dos Reis, R.; Hsu, S. L.; Xiao, J.; Zhang, H.; Wagner, R.; Datar, A.; McCarter, M. R.; Serrao, C. R.; Yadav, A. K.; Karbasian, G.; Hsu, C. H.; Tan, A. J.; Wang, L. C.; Thakare, V.; Zhang, X.; Mehta, A.; Karapetrova, E.; Chopdekar, R. V.; Shafer, P.; Arenholz, E.; Hu, C.; Proksch, R.; Ramesh, R.; Ciston, J.; Salahuddin, S. Enhanced Ferroelectricity in Ultrathin Films Grown Directly on Silicon. *Nature* **2020**, *580*, 478−482.

(18) Kang, L.; Jiang, P.; Cao, N.; Hao, H.; Zheng, X.; Zhang, L.; Zeng, Z. Realizing Giant Tunneling Electroresistance in Two-Dimensional Graphene/Bip Ferroelectric Tunnel Junction. *Nanoscale* **2019**, *11*, 16837−16843.

(19) Wu, J.; Chen, H.-Y.; Yang, N.; Cao, J.; Yan, X.; Liu, F.; Sun, Q.; Ling, X.; Guo, J.; Wang, H. High Tunnelling Electroresistance in a Ferroelectric Van Der Waals Heterojunction Via Giant Barrier Height Modulation. *Nat. Electron.* **2020**, *3*, 466−472.

(20) Lee, D.; Yoon, A.; Jang, S. Y.; Yoon, J. G.; Chung, J. S.; Kim, M.; Scott, J. F.; Noh, T. W. Giant Flexoelectric Effect in Ferroelectric Epitaxial Thin Films. *Phys. Rev. Lett.* **2011**, *107*, No. 057602.
(21) Das, S.; Wang, B.; Paudel, T. R.; Park, S. M.; Tsymbal, E. Y.; Chen, L.-Q.; Lee, D.; Noh, T. W. Enhanced Flexoelectricity at Reduced Dimensions Revealed by Mechanically Tunable Quantum Tunnelling. *Nat. Commun.* **2019**, *10*, No. 537.
(22) Yang, M.-M.; Kim, D. J.; Alexe, M. Flexo-Photovoltaic Effect. *Science* **2018**, *360*, 904.
(23) Lu, H.; Bark, C.-W.; Esque de los Ojos, D.; Alcala, J.; Eom, C. B.; Catalan, G.; Gruverman, A. Mechanical Writing of Ferroelectric Polarization. *Science* **2012**, *336*, 59−61.
(24) Li, Y.-J.; Wang, J.-J.; Ye, J.-C.; Ke, X.-X.; Gou, G.-Y.; Wei, Y.; Xue, F.; Wang, J.; Wang, C.-S.; Peng, R.-C.; Deng, X.-L.; Yang, Y.; Ren, X.-B.; Chen, L.-Q.; Nan, C.-W.; Zhang, J.-X. Mechanical Switching of Nanoscale Multiferroic Phase Boundaries. *Adv. Funct. Mater.* **2015**, *25*, 3405−3413.
(25) Gao, P.; Yang, S.; Ishikawa, R.; Li, N.; Feng, B.; Kumamoto, A.; Shibata, N.; Yu, P.; Ikuhara, Y. , Atomic-Scale Measurement of Flexoelectric Polarization at ${\Mathrm{Srtio}}_{3}$ Dislocations. *Phys. Rev. Lett.* **2018**, *120*, No. 267601.
(26) Ma, J.; Ma, J.; Zhang, Q.; Peng, R.; Wang, J.; Liu, C.; Wang, M.; Li, N.; Chen, M.; Cheng, X.; Gao, P.; Gu, L.; Chen, L.-Q.; Yu, P.; Zhang, J.; Nan, C.-W. Controllable Conductive Readout in Self-Assembled, Topologically Confined Ferroelectric Domain Walls. *Nat. Nanotechnol.* **2018**, *13*, 947−952.
(27) Ma, J.; Wang, J.; Zhou, H.; Zhang, Q.; Liang, Y.; Chen, M.; Gu, L.; Xu, B.; Zhang, J.; Ma, J.; Nan, C.-W. Self-Assembly Growth of a Multiferroic Topological Nanoisland Array. *Nanoscale* **2019**, *11*, 20514−20521.
(28) Wang, J.; Ma, J.; Yang, Y.; Chen, M.; Zhang, J.; Ma, J.; Nan, C.-W. Ferroelectric Photodetector with High Current on−Off Ratio (∼1 × 10^4%) in Self-Assembled Topological Nanoislands. *ACS Appl. Electron. Mater.* **2019**, *1*, 862−868.
(29) Wang, J.; Huang, H.; He, W.; Zhang, Q.; Yang, D.; Zhang, Y.; Liang, R.; Wang, C.; Ma, X.; Gu, L.; Chen, L.; Nan, C.-W.; Zhang, J. Nanoscale Bandgap Tuning across an Inhomogeneous Ferroelectric Interface. *ACS Appl. Mater. Interfaces* **2017**, *9*, 24704−24710.
(30) Seidel, J.; Martin, L. W.; He, Q.; Zhan, Q.; Chu, Y. H.; Rother, A.; Hawkridge, M. E.; Maksymovych, P.; Yu, P.; Gajek, M.; Balke, N.; Kalinin, S. V.; Gemming, S.; Wang, F.; Catalan, G.; Scott, J. F.; Spaldin, N. A.; Orenstein, J.; Ramesh, R. Conduction at Domain Walls in Oxide Multiferroics. *Nat. Mater.* **2009**, *8*, 229−234.
(31) Yang, M.-M.; Iqbal, A. N.; Peters, J. J. P.; Sanchez, A. M.; Alexe, M. Strain-Gradient Mediated Local Conduction in Strained Bismuth Ferrite Films. *Nat. Commun.* **2019**, *10*, No. 2791.
(32) Lu, H.; Lee, D.; Klyukin, K.; Tao, L.; Wang, B.; Lee, H.; Lee, J.; Paudel, T. R.; Chen, L.-Q.; Tsymbal, E. Y.; Alexandrov, V.; Eom, C.-B.; Gruverman, A. Tunneling Hot Spots in Ferroelectric Srtio3. *Nano Lett.* **2018**, *18*, 491−497.
(33) Gu, Y.; Li, M.; Morozovska, A. N.; Wang, Y.; Eliseev, E. A.; Gopalan, V.; Chen, L.-Q. Flexoelectricity and Ferroelectric Domain Wall Structures: Phase-Field Modeling and Dft Calculations. *Phys. Rev. B: Condens. Matter Mater. Phys.* **2014**, *89*, No. 174111.
(34) Wang, Y. J.; Tang, Y. L.; Zhu, Y. L.; Feng, Y. P.; Ma, X. L. Converse Flexoelectricity around Ferroelectric Domain Walls. *Acta Mater.* **2020**, *191*, 158−165.
(35) Rojac, T.; Bencan, A.; Drazic, G.; Sakamoto, N.; Ursic, H.; Jancar, B.; Tavcar, G.; Makarovic, M.; Walker, J.; Malic, B.; Damjanovic, D. Domain-Wall Conduction in Ferroelectric Bifeo3 Controlled by Accumulation of Charged Defects. *Nat. Mater.* **2017**, *16*, 322−327.
(36) Tian, G.; Yang, W.; Song, X.; Zheng, D.; Zhang, L.; Chen, C.; Li, P.; Fan, H.; Yao, J.; Chen, D.; Fan, Z.; Hou, Z.; Zhang, Z.; Wu, S.; Zeng, M.; Gao, X.; Liu, J. M. Manipulation of Conductive Domain Walls in Confined Ferroelectric Nanoislands. *Adv. Funct. Mater.* **2019**, *29*, No. 1807276.
(37) Han, M. J.; Tang, Y. L.; Wang, Y. J.; Zhu, Y. L.; Ma, J. Y.; Geng, W. R.; Feng, Y. P.; Zou, M. J.; Zhang, N. B.; Ma, X. L. Charged Domain Wall Modulation of Resistive Switching with Large on/Off Ratios in High Density Bifeo3 Nano-Islands. *Acta Mater.* **2020**, *187*, 12−18.
(38) Maksymovych, P.; Jesse, S.; Yu, P.; Ramesh, R.; Baddorf, A. P.; Kalinin, S. V. Polarization Control of Electron Tunneling into Ferroelectric Surfaces. *Science* **2009**, *324*, 1421−1425.
(39) Wang, J.; Yang, H.; Wang, Y.; Fan, Y.; Liu, D.; Yang, Y.; Wu, J.; Chen, M.; Gao, R.; Huang, H.; et al. Polarization-Switching Pathway Determined Electrical Transport Behaviors in Rhombohedral Bifeo 3 Thin Films. *Nanoscale* **2021**, *13*, 17746−17753.
(40) Wang, J.; Fan, Y.; Song, Y.; Wu, J.; Zhu, R.; Gao, R.; Shao, C.; Huang, H.; Gao, P.; Xu, B.; Ma, J.; Zhang, J.; Nan, C.-W. Microscopic Physical Origin of Polarization Induced Large Tunneling Electroresistance in Tetragonal-Phase Bifeo3. *Acta Mater.* **2022**, *225*, No. 117564.
(41) Seidel, J.; Maksymovych, P.; Batra, Y.; Katan, A. J.; Ramesh, R.; et al. Domain Wall Conductivity in La-Doped Bifeo3. *Phys. Rev. Lett.* **2010**, *105*, No. 197603.
(42) Simmons, J. G. Poole-Frenkel Effect and Schottky Effect in Metal-Insulator-Metal Systems. *Phys. Rev.* **1967**, *155*, 657−660.
(43) Li, Y. J.; Wang, J. J.; Ye, J. C.; Ke, X. X.; Gou, G. Y.; Wei, Y.; Xue, F.; Wang, J.; Wang, C. S.; Peng, R. C.; et al. Mechanical Switching of Nanoscale Multiferroic Phase Boundaries. *Adv. Funct. Mater.* **2015**, *25*, 3405−3413.
(44) Yang, M.; Iqbal, A. N.; Peters, J.; Sanchez, A. M.; Alexe, M.; et al. Strain-Gradient Mediated Local Conduction in Strained Bismuth Ferrite Films. *Nat. Commun.* **2019**, *10*, 2791.
(45) Jin Hu, W.; Wang, Z.; Yu, W.; Wu, T.; et al. Optically Controlled Electroresistance and Electrically Controlled Photovoltage in Ferroelectric Tunnel Junctions. *Nat. Commun.* **2016**, *7*, 10808.
(46) Glass, A. M.; Linde, D. vd.; Negran, T. J. High-Voltage Bulk Photovoltaic Effect and the Photorefractive Process in Linbo3. *Appl. Phys. Lett.* **1974**, *25*, 233−235.
(47) Baek, S.; Jang, H.; Folkman, C.; Li, Y.; Winchester, B.; Zhang, J.; He, Q.; Chu, Y.; Nelson, C.; Rzchowski, M.; et al. Ferroelastic Switching for Nanoscale Non-Volatile Magnetoelectric Devices. *Nat. Mater.* **2010**, *9*, 309.
(48) Bai, Z. L.; Cheng, X. X.; Chen, D. F.; Zhang, D. W.; Chen, L.-Q.; Scott, J. F.; Hwang, C. S.; Jiang, A. Q. Hierarchical Domain Structure and Extremely Large Wall Current in Epitaxial Bifeo3 Thin Films. *Adv. Funct. Mater.* **2018**, *28*, No. 1801725.
(49) Liang, F.; Lu, Y.; Yang, Z.; Peng, R.; Zhi, S. L.; Wang, J. Switchable Photovoltaic Response from Polarization Modulated Interfaces in Bifeo3 Thin Films. *Appl. Phys. Lett.* **2014**, *104*, No. 142903.

https://doi.org/10.1021/acsami.1c25259
ACS Appl. Mater. Interfaces 2022, 14, 18662−18670